

A mechanism for mode selection in melt band instabilities

David Bercovici^{a,*}, John F. Rudge^b

^a*Yale University, Department of Geology & Geophysics, New Haven CT, USA*

^b*Bullard Laboratories, Department of Earth Sciences, University of Cambridge, Madingley Road, Cambridge CB3 0EZ, United Kingdom*

Abstract

The deformation of partially molten mantle in tectonic environments can lead to exotic structures, which potentially affect both melt and plate-boundary focussing. Examples of such structures are found in laboratory deformation experiments on partially molten rocks. Simple-shear and torsion experiments demonstrate the formation of concentrated melt bands at angles of around 20° to the shear plane. The melt bands form in the experiments with widths between a few to tens of microns, and a band spacing roughly an order of magnitude larger. Existing compaction theories, however, cannot predict this band width structure, let alone any mode selection, since they infer the fastest growing instability to occur for wavelengths or bands of vanishing width. Here, we propose that surface tension in the mixture, especially on a diffuse interface in the limit of sharp melt-fraction gradients, can mitigate the instability at vanishing wavelength and thus permit mode selection for finite-width bands. Indeed, the expected weak capillary forces on the diffuse interface lead to predicted mode selection at the melt-band widths observed in the experiments.

Keywords: Magma transport; mantle dynamics; rock deformation

1. Introduction

While mantle melting only occurs within a small volume of the Earth, it plays a disproportionate role in both geochemical evolution and plate-boundary processes (see [Cox et al., 1993](#)). Indeed, the unique deformation of partial melts likely controls flow and strain

*Corresponding author

Email addresses: david.bercovici@yale.edu (David Bercovici), jfr23@cam.ac.uk (John F. Rudge)

5 focussing at both convergent and divergent plate boundaries (e.g., [Spiegelman and McKenzie, 1987](#); [Katz, 2008](#); [Gerya and Meilick, 2011](#); [Gerya, 2013](#)). In particular, sheared partial melts have been demonstrated in laboratory experiments ([Daines and Kohlstedt, 1997](#);
6 [Holtzman et al., 2003](#); [King et al., 2010](#); [Qi et al., 2013](#)) to develop narrow melt bands at
7 shallow angles ($\sim 20^\circ$) to the direction of motion. Such melt banding may provide high-
8 permeability pathways that strongly influence the transport of melt to the Earth's surface
9 ([Kohlstedt and Holtzman, 2009](#)).

12 The observed shallow angle of these melt bands is enigmatic and has been the subject of
13 several theoretical studies invoking two-phase compaction theory with various rheological
14 mechanisms ([Stevenson, 1989](#); [Spiegelman, 2003](#); [Katz et al., 2006](#); [Takei and Holtzman, 2009](#);
15 [Butler, 2012](#); [Takei and Katz, 2013](#); [Katz and Takei, 2013](#); [Rudge and Bercovici, 2015](#)). An equally significant enigma is that current two-phase models cannot predict the
16 basic melt band width, since they infer the fastest growing instability to have zero wave-
17 length. Laboratory experiments, however, show that while the melt bands are very narrow,
18 of order a few to tens of microns wide, and with band spacing roughly an order of magni-
19 tude wider ([Holtzman et al., 2003](#); [Holtzman and Kohlstedt, 2007](#); [Kohlstedt and Holtzman, 2009](#)),
20 they are consistently not vanishingly small. The failure to predict mode selection
21 has been a significant conundrum for understanding the physics let alone believing the
22 theories, and is problematic for numerical simulations for which instabilities shrink to the
23 grid-scale, and thus cannot be resolved ([Katz et al., 2006](#); [Butler, 2012](#); [Alisic et al., 2014](#)).
24 [Butler \(2010\)](#) proposed that, in the finite strain limit, the rotation of bands through the
25 optimal angle of growth can amplify larger wavelength bands, although as shown earlier
26 by [Spiegelman \(2003\)](#) this effect depends on the initial conditions for the structure of the
27 porosity perturbations. [Takei and Hier-Majumder \(2009\)](#) proposed that compaction coin-
28 cident with dissolution and precipitation provides mode selection governed by a chemical
29 diffusion length scale, which is indeed similar to the widest band spacing, although not the
30 band widths. However, while such chemical reactions between phases are expected to be
31

important in geological settings (Aharonov et al., 1997), their role was not evident in the laboratory experiments, which were designed to study melt channels by stress alone and avoid reaction channelization (Holtzman et al., 2003).

Here we consider two-phase compaction theory that includes capillary effects from the interface between phases, i.e., the melt and matrix (Stevenson, 1986; Bercovici et al., 2001; Bercovici and Ricard, 2003; Hier-Majumder et al., 2006), as a means for explaining mode selection. However, capillary effects at the microscopic (i.e., pore/grain) scale cannot give the necessary effect (as will be demonstrated herein). In this paper, we propose a small adjustment to existing theories that involves a diffuse interface effect, which occurs at very large gradients in melt volume fraction (e.g., Sun and Beckermann, 2004). Below we briefly develop the concept of the diffuse interface coincident with microscopic interfaces, and demonstrate how it can predict mode selection at the observed melt-band wavelengths.

2. Theory

2.1. Two-phase mixture interface and diffuse interface

Various two-phase flow theories treat the interface between phases and associated surface energy and surface tension by defining an interface area density (i.e., interface area per unit volume) α (see Ni and Beckerman, 1991; Bercovici et al., 2001). For example, if a volume δV of mixture is filled with N spherical fluid bubbles of radius r , surrounded by an opposite matrix phase, then the fluid volume fraction is $\phi = N\frac{4}{3}\pi r^3/\delta V$, while $\alpha = N4\pi r^2/\delta V$; in the same vein, the average curvature of this interface would be $d\alpha/d\phi = (d\alpha/dr)/(d\phi/dr) = 2/r$ as expected.

However if the mixture has sharp gradients in fluid fraction $\nabla\phi$, then the gradient region itself can appear as an effective or diffuse interface. Sun and Beckermann (2004) consider a diffuse interface in a mixture and invoke the formalism of phase-field theory (Anderson et al., 1998; Chen, 2002; Moelans et al., 2008) to propose an adjusted model for

interface density and curvature. We appeal to some of their concepts but diverge in other respects. One important deviation is that phase-field theory only has interfaces defined by gradients in the phase variable, while we have both a background interface from a more homogeneous distribution of phases (i.e., bubbles and grains) in addition to an effective diffuse interface caused by sharp gradients in the fluid volume fraction.

Although the interface density α may be affected by a diffuse interface, only the curvature appears in the dynamics and thus we need only specify how $d\alpha/d\phi$ is altered. Indeed as shown in §[Appendix A](#), we infer an effective curvature

$$\frac{d\alpha}{d\phi} = \frac{d\mathcal{A}}{d\phi} - \frac{1}{\mathcal{A}} \nabla^2 \phi \quad (1)$$

where \mathcal{A} is the microscopic (pore and grain) scale interface area, which we assume is only a function of porosity (see [Bercovici et al., 2001](#); [Hier-Majumder et al., 2006](#)). The two terms on the right of (1) are due to microscopic scale interface curvature originally described by [Bercovici et al. \(2001\)](#) (first term), and that due to sharp coherent structures in the porosity field (second term). For example, a coherent structure with a sharp gradient in porosity can resemble a macroscopic bubble wall separating low and high porosity regions, which then has a net effective surface tension on it. However, there is a continuum of coherent structures between weak gradients for which the diffuse interface will barely register, to sharper ones. Indeed, since \mathcal{A} is a large zeroth-order term, the diffuse interface curvature term only becomes important for sharp gradients in ϕ . Equation (1) is the same as the mean curvature inferred by [Sun and Beckermann \(2004\)](#), however we diverge from those authors by retaining (1) as the full effective interface curvature, while they argue to remove the microscale curvature, i.e., the first term on the right of (1). We retain this term since it is responsible for driving phase self-separation and/or wetting. Indeed the 2nd term retards self-separation once the porosity gradients get very large, and leads to a steady state separation rather than run-away separation. But to allow initial capillary effects on the

81 pore or grain scale, we retain the micro-scale curvature term. In the end, the new effective
 82 interface curvature $d\alpha/d\phi$ can be employed in the appropriate two-phase theory (Bercovici
 83 et al., 2001; Bercovici and Ricard, 2003).

84 2.2. Mass conservation

85 Conservation of mass in two-phase continuum mechanics dictates a relation for the
 86 volume fraction ϕ_i of phase i (i.e., either phase), which, assuming both phases are incom-
 87 pressible and there is no mass exchange between phases, leads to

$$\frac{\partial \phi_i}{\partial t} + \nabla \cdot (\phi_i \mathbf{v}_i) = 0 \quad (2)$$

88 where \mathbf{v}_i is the velocity of phase i . Summing these equations and noting that $\sum_i \phi_i = 1$,
 89 we arrive at

$$\nabla \cdot \bar{\mathbf{v}} = 0 \quad (3)$$

90 where $\bar{\mathbf{v}} = \sum_i \phi_i \mathbf{v}_i$. We can also define the unsubscripted $\phi = \phi_1$ as the volume fraction
 91 of the minor phase, here the fluid or melt phase. We also define the unsubscripted $\mathbf{v} = \mathbf{v}_2$
 92 as the velocity of the solid or matrix phase, and $\Delta \mathbf{v} = \mathbf{v}_2 - \mathbf{v}_1$ as the phase separation
 93 velocity. We can hence recast (2) and (3) as

$$\frac{D\phi}{Dt} = (1 - \phi) \nabla \cdot \mathbf{v} \quad (4)$$

94 and

$$\nabla \cdot \bar{\mathbf{v}} = \nabla \cdot (\mathbf{v} - \phi \Delta \mathbf{v}) = 0 \quad (5)$$

95 where $D/Dt = \partial/\partial t + \mathbf{v} \cdot \nabla$ is the material derivative in the matrix frame of reference.

96 2.3. Dynamics

97 The conservation of momentum in a creeping two-phase medium is generally pre-
98 scribed (following [Bercovici and Ricard, 2003, 2012](#))

$$0 = -\phi_i \nabla \Pi_i + \nabla \cdot (\phi_i \underline{\tau}_i) \pm c \Delta \mathbf{v} + \omega_i (\Delta \Pi \nabla \phi + \nabla (\gamma \alpha)) \quad (6)$$

99 where we neglect gravity for the application at hand, and where the internal pressure on
100 phase i is Π_i , $\underline{\tau}_i$ is the deviatoric stress tensor in phase i , phase density is ρ_i , c is the
101 coefficient of drag between phases, $\Delta \Pi = \Pi_2 - \Pi_1$, γ is the surface tension on the interface
102 between phases, α is again the interface density, and ω_i is a weighting factor (such that
103 $\sum_i \omega_i = 1$) that accounts for how much surface tension is embedded in one phase relative
104 to the other.

105 2.3.1. Constitutive laws and rheology

106 Since phase 1 is a melt we assume $\underline{\tau}_1 \approx 0$ and $\omega_1 = 0$ ([Bercovici and Ricard, 2003](#)).
107 The matrix deviatoric stress is thus denoted as $\underline{\tau} = \underline{\tau}_2$ and given by

$$\underline{\tau} = 2\mu \underline{\dot{\epsilon}} = \mu \left(\nabla \mathbf{v} + [\nabla \mathbf{v}]^t - \frac{2}{3} \nabla \cdot \mathbf{v} \underline{\mathbf{I}} \right) \quad (7)$$

108 where μ is the matrix viscosity, and $\underline{\dot{\epsilon}}$ is the matrix deviatoric strain-rate tensor, $[..]^t$ implies
109 tensor transpose and $\underline{\mathbf{I}}$ is the identity tensor. In keeping with prior analysis ([Katz et al.,](#)
110 [2006](#)), we allow that $(1 - \phi)\mu$ is an effective viscosity given generally by

$$\mu_{\text{eff}} = (1 - \phi)\mu = \mu_0 \Lambda(\phi, \dot{\epsilon}^2) = \mu_0 e^{-b(\phi - \phi_0)} \left(\frac{\dot{\epsilon}^2}{\dot{\epsilon}_0^2} \right)^{\frac{1-n}{2n}} \quad (8)$$

111 where n is a true or effective power-law index, b is a constant, ϕ_0 is a reference melt fraction,
112 and $\dot{\epsilon}^2 = \frac{1}{2} \underline{\dot{\epsilon}} : \underline{\dot{\epsilon}}$: $\underline{\dot{\epsilon}}$ is the 2nd strain-rate invariant, which has a reference or imposed value
113 $\dot{\epsilon}_0^2$. This rheology allows for either a dislocation creep power-law rheology where $n \approx 3$

114 (Katz et al., 2006), or an effective power-law rheology from grain-damage in which n can
 115 be larger than 3 (Rudge and Bercovici, 2015). Finally, significant banding instabilities
 116 appear to require a strongly nonlinear porosity-dependent viscosity, e.g., with $b \approx 25/n$
 117 (Mei et al., 2002; Katz et al., 2006; Takei and Holtzman, 2009).

118 The constitutive law for the pressure difference across the interface is given by (Bercovici
 119 and Ricard, 2003)

$$\Delta\Pi = -\gamma\frac{d\alpha}{d\phi} - B(\phi)\frac{D\phi}{Dt} \quad (9)$$

120 where the 2nd term on the right accounts for viscous resistance to matrix compaction, thus
 121 B is akin to the effective bulk viscosity invoked by McKenzie (1984), and is in general a
 122 function of ϕ .

123 The interface drag coefficient is denoted by c and is typically proportional to the ratio of
 124 melt viscosity to matrix permeability; however, for the sake of simplicity there is no need
 125 to introduce a new variable yet, and we merely need to note that c is also a function of ϕ .

126 2.4. Final synthesized force balance equations

127 Given the assumption of inviscid melt, the force balance equation (6) for the melt (phase
 128 1) essentially becomes Darcy's law:

$$0 = -\nabla P + c\Delta\mathbf{v}/\phi \quad (10)$$

129 where we define $\Pi_1 = P$ is the fluid (melt) pressure. The weighted difference of the two
 130 momentum equations (i.e., $\phi_1 = \phi$ times the equation for phase 2 minus $\phi_2 = 1 - \phi$ times
 131 the equation for phase 1) leads to

$$0 = \nabla (\mathcal{B}\nabla \cdot \mathbf{v}) + 2\mu_0\nabla \cdot (\Lambda\dot{\underline{\epsilon}}) - c\Delta\mathbf{v}/\phi + \gamma\nabla \left(\alpha + (1 - \phi)\frac{d\alpha}{d\phi} \right) \quad (11)$$

132 where we define $\mathcal{B} = (1 - \phi)^2 B(\phi)$. Using the arguments outlined in §2.1, the last term on
 133 the right of (11) is

$$\gamma \nabla \left(\alpha + (1 - \phi) \frac{d\alpha}{d\phi} \right) = \gamma(1 - \phi) \left(\frac{d^2 \mathcal{A}}{d\phi^2} \nabla \phi - \frac{1}{\mathcal{A}} \nabla (\nabla^2 \phi) + \frac{1}{\mathcal{A}^2} \frac{d\mathcal{A}}{d\phi} (\nabla^2 \phi) \nabla \phi \right) \quad (12)$$

134 The first term on the right side of (12) provides an effective pressure gradient due to vari-
 135 ations in microscopic interface curvature, which can, depending on the sign of $d^2 \mathcal{A}/d\phi^2$,
 136 either lead to self-separation of phases (if the sign is negative; see Ricard et al., 2001;
 137 Bercovici and Ricard, 2003) or dispersal of phases via wetting of grain-boundaries (if the
 138 sign is positive; see Hier-Majumder et al., 2006) as generally happens in low-melt fraction
 139 partial melts (e.g., Parsons et al., 2008; King et al., 2011, and references therein). The
 140 second two terms on the right of (12) together represent a pressure gradient caused by vari-
 141 ations in the surface tension on effective macroscopic (diffuse) interfaces associated with
 142 sharp gradients in ϕ . In particular, high pressure zones are caused by the surface tension
 143 around porosity anomalies with large functional curvature $\nabla^2 \phi$ (which thus act, for ex-
 144 ample, like effective bubbles of high porosity), and the resulting pressure gradient acts to
 145 smooth out the porosity anomalies and mitigate the development of sharp porosity features.
 146 However the nonlinear contributions to this effect, in particular the third term on the right
 147 of (12), do not influence the linear stability analysis presented herein.

148 3. Linear analysis of simple shear experiments

149 As a representation of the shear-band experiments (Holtzman et al., 2003; Kohlstedt
 150 and Holtzman, 2009), we assume the model system is in simple shear in the x direction
 151 with steady velocity given by

$$\mathbf{v}_0 = u(y) \hat{\mathbf{x}} = 2y \dot{\epsilon}_0 \hat{\mathbf{x}} \quad (13)$$

152 where $\dot{\epsilon}_0$ is an imposed shear strain-rate. The basic steady state is assumed uniform and
 153 constant, with no phase separation (i.e., both phases move at velocity \mathbf{v}_0). We consider
 154 two-dimensional (2-D) infinitesimal perturbations to the basic state in the horizontal x - y
 155 plane, in which case, the dependent variables become

$$156 \quad \phi = \phi_0 + \epsilon \varphi_1 \quad (14a)$$

$$157 \quad \mathbf{v} = \mathbf{v}_0(y) + \epsilon(\nabla \vartheta_1 + \nabla \times (\psi_1 \hat{\mathbf{z}})) \quad (14b)$$

$$158 \quad \Delta \mathbf{v} = \epsilon \Delta \mathbf{v}_1 \quad (14c)$$

$$159 \quad \Lambda = \Lambda_0 + \epsilon \Lambda_1 = 1 - \epsilon \left(b \varphi_1 + q \frac{\dot{\epsilon}_{1xy}}{\dot{\epsilon}_0} \right) \quad (14d)$$

161 where $\epsilon \ll 1$, ϑ_1 is a flow potential, ψ_1 is a stream function, and $q = 1 - 1/n$. All zeroth
 162 order variables are uniform and constant except for \mathbf{v}_0 which is a function of y , and all first
 163 order variables are functions of x , y and time t . We first substitute (14) into (4), and into
 164 both $\nabla \cdot$ and $\hat{\mathbf{z}} \cdot \nabla \times$ of (11), using (5) and (10) to eliminate $\Delta \mathbf{v}$. This yields governing
 165 equations for the perturbations of $O(\epsilon^1)$, which we then non-dimensionalize by scaling
 166 time by $(2\dot{\epsilon}_0)^{-1}$, and distance by the compaction length

$$\delta = \sqrt{\phi_0^2 (\mathcal{B}_0 + \frac{4}{3} \mu_0) / c_0} \quad (15)$$

167 where $\mathcal{B}_0 = \mathcal{B}(\phi_0)$ and $c_0 = c(\phi_0)$. The dimensionless governing perturbation equations
 168 become, after some algebra

$$169 \quad \frac{D_0 \varphi_1}{Dt} = (1 - \phi_0) \nabla^2 \vartheta_1 \quad (16a)$$

$$170 \quad (\nabla^4 - \nabla^2) \vartheta_1 = \nu \left(\Gamma (\mathcal{D} \nabla^4 - \nabla^2) \varphi_1 - 2 \frac{\partial^2 \Lambda_1}{\partial x \partial y} \right) \quad (16b)$$

$$171 \quad \nabla^4 \psi_1 = \Delta^* \Lambda_1 \quad (16c)$$

$$172 \quad \Lambda_1 = -b \varphi_1 + q \left(\Delta^* \psi_1 - 2 \frac{\partial^2 \vartheta_1}{\partial x \partial y} \right) \quad (16d)$$

173 where $\Delta^* = \frac{\partial^2}{\partial x^2} - \frac{\partial^2}{\partial y^2}$, and

$$175 \quad \nu = \frac{\mu_0}{\mathcal{B}_0 + \frac{4}{3} \mu_0} \quad (17a)$$

$$176 \quad \Gamma = \frac{\gamma(1 - \phi_0) \mathcal{A}_0''}{2 \hat{\varepsilon}_0 \mu_0} \quad (17b)$$

$$177 \quad \mathcal{D} = (\mathcal{A}_0'' \mathcal{A}_0 \delta^2)^{-1} \quad (17c)$$

178 in which $\mathcal{A}_0 = \mathcal{A}(\phi_0)$ and $\mathcal{A}_0'' = [d^2 \mathcal{A} / d\phi^2]_{\phi_0}$.

180 3.1. Normal mode analysis and dispersion relation

181 In the usual method of normal mode analysis, we assume all dependent variables go as
 182 $e^{-i\mathbf{k} \cdot \mathbf{x} + st}$ where $\mathbf{k} = (k_x, k_y) = k(\cos \theta, \sin \theta)$ is the wave vector in which θ is the wave-
 183 vector angle, $\mathbf{x} = (x, y)$ is the position vector, and s is the growth rate. Substituting this
 184 relation into (16), and solving for s leads to the dispersion relation

$$s = (1 - \phi_0) \nu \Gamma k^2 \cdot \frac{\mathcal{Q} \sin(2\theta) - (1 + \mathcal{D} k^2) (1 - q \cos^2(2\theta))}{(1 + k^2) (1 - q \cos^2(2\theta)) - q \nu k^2 \sin^2(2\theta)} \quad (18)$$

185 where we define $\mathcal{Q} = b/\Gamma$ (see Figure 1). Here we have neglected the advection term
 186 in (16a); inclusion of advection does not change the basic results but simply breaks the

187 degeneracy of mode selection in θ in favor of shallow-angled bands (Spiegelman, 2003;
188 Katz et al., 2006; Rudge and Bercovici, 2015).

189 The influence of shear deformation is represented in the numerator of (18) by the term
190 that goes as $\Gamma \mathcal{Q} = b$, modulated by non-Newtonian effects in the denominator, but which
191 is then always positive. The effect of surface tension is contained in the factor that goes as
192 $\Gamma + \Gamma \mathcal{D} k^2$, whose two terms represent microscopic and diffuse-interface capillary effects,
193 respectively. Only the microscopic capillary term depends on microscopic interface curva-
194 ture \mathcal{A}_0'' , which can either be negative for self-separation (Ricard et al., 2001) (that would
195 then accelerate the banding instability), or positive for wetting and melt dispersal (Hier-
196 Majumder et al., 2006) (that then, like the diffuse-interface effect, retards the instability).
197 Here we assume $\mathcal{A}_0'' > 0$ for the wetting case, which is typical of partial melts (Parsons et al.,
198 2008; King et al., 2011). However, only the diffuse interface effect permits mode selection.
199 For example, in the limits of $k^2 \rightarrow 0$ and $k^2 \rightarrow \infty$, $s \rightarrow 0$ and $s \rightarrow -\infty$, respectively,
200 but has positive values in between these limits, and thus a least-stable mode exists at some
201 finite k . If there is no diffuse interface effect such that $\mathcal{D} = 0$, then s goes to a positive
202 asymptote as $k^2 \rightarrow \infty$ and there is no selected mode (Figure 1). Thus only the introduction
203 of diffuse interface surface tension allows for mode selection at finite wavelength; micro-
204 scopic capillary forces (even if causing wetting and melt dispersal) by themselves will not
205 allow for mode selection. Although the mode selection is very broad for expected param-
206 eter values, in which $\mathcal{Q} \gg 1$ and $\mathcal{D} \ll 1$ (Figure 1) these same parameters lead to a very
207 high wavenumber k , or small wavelength, selection, as discussed next.

208 3.1.1. Least stable mode

209 We can gain some immediate intuition about mode selection if we first consider the
210 simplest case of a Newtonian matrix rheology, whence $q = 0$, in which case the growth

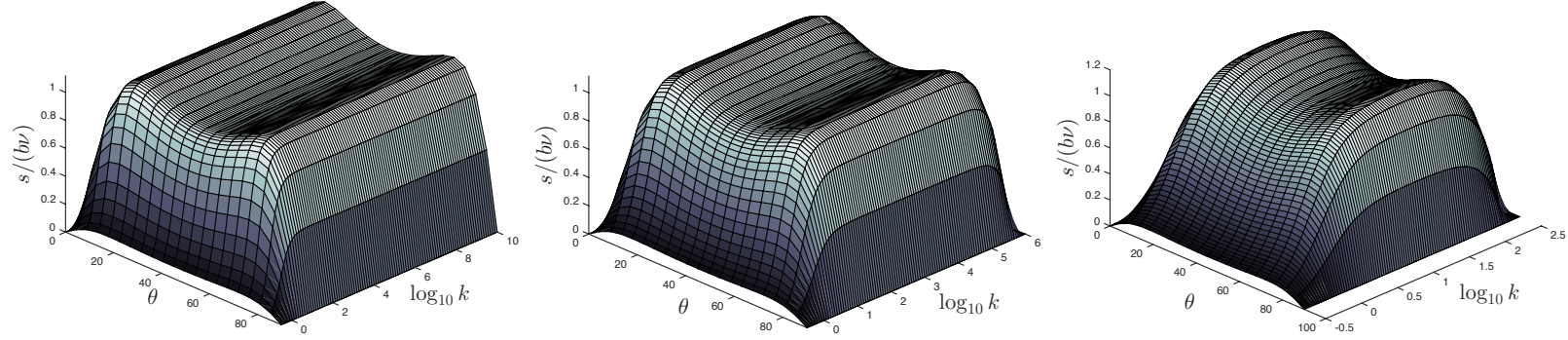


Figure 1: Growth s vs wave-number k and wave-vector angle θ from (18). The left and middle panels are for $\mathcal{D} = 0$ and $\mathcal{D} = 10^{-8}$, respectively, and both have $\mathcal{Q} = b/\Gamma = 10^4$ (the left panel is also arbitrarily truncated at $k = 10^{10}$); the right panel is for $\mathcal{Q} = 10^3$ and $\mathcal{D} = 10^{-2}$. The case for $\mathcal{D} = 0$ (left panel) does not have peak growth at a finite k and thus does not allow mode selection, unlike the cases for $\mathcal{D} > 0$. All three cases have the same values of $\phi_0 = 0.05$, $n = 4$, $\nu = 3\phi_0/4$.

rate is necessarily maximum at $\theta = \pi/4$ (i.e., bands at 45° angles), and thus

$$s = (1 - \phi_0)\nu\Gamma k^2 \cdot \frac{\mathcal{Q} - (1 + \mathcal{D}k^2)}{1 + k^2} \quad (19)$$

Marginal stability occurs for $s = 0$, which implies a critical value of $\mathcal{Q} = 1 + \mathcal{D}k^2$ above which perturbations are unstable. The least stable mode, for which $ds/dk^2 = 0$, occurs at a wave-number given by

$$k_m^2 = \sqrt{1 + (\mathcal{Q} - 1)/\mathcal{D}} - 1 \quad (20)$$

However, as discussed in §4.1, typical experimental conditions and properties lead to $\mathcal{Q} \gg 1$ and $\mathcal{D} \ll 1$ and thus $k_m \approx (\mathcal{Q}/\mathcal{D})^{1/4}$, which, while not infinite, is intrinsically a large number and thus leads to small wavelengths. At this wavenumber, the approximate growth rate from (19) (noting that typically $\mathcal{Q}\mathcal{D} \ll 1$ such that $\mathcal{D}k^2 \ll 1$) is $s_m \approx (1 - \phi_0)b\nu$, which is typically $O(1)$ (again see §4.1), and thus the dimensional growth rate is roughly equal to the imposed strain-rate. These simple scaling results for the least stable mode and associated growth rate hold for the general case except for an angular dependence as well as influence of $q \neq 0$, for which the least stable mode does not occur at $\theta = \pi/4$.

223 For the general case of $q \neq 0$ and arbitrary fixed θ , the least stable mode is given by

$$k_m^2 = \frac{\sqrt{1 + \frac{1}{D} \left(\frac{QS}{C^2} - 1 \right) \left(1 - \frac{q\nu S^2}{C^2} \right)} - 1}{1 - \frac{q\nu S^2}{C^2}} \quad (21)$$

224 where we have defined

$$S = \sin(2\theta) \text{ and } C^2 = 1 - q \cos^2(2\theta) \quad (22)$$

225 (see Figure 2). Again, taking the asymptotic limits $Q \gg 1$ and $D \ll 1$, and in addition
 226 $q\nu S^2/C^2 \ll 1$ (since $\nu \sim \phi_0 \ll 1$; see §4.1), the least-stable wave-number and associated
 227 growth rate are

$$k_m \approx \left(\frac{QS}{DC^2} \right)^{1/4} \text{ and } s_m \approx (1 - \phi_0) \frac{b\nu S}{C^2} \quad (23)$$

228 (see Figure 2).

229 The dependences on θ and $q = 1 - 1/n$ for both k_m and s_m are contained in the ratio
 230 S/C^2 . Thus the angle θ at which maximum growth occurs is given by $d(SC^{-2})/d\theta = 0$
 231 which leads to $\theta_m = \frac{1}{2} \sin^{-1}(\pm \sqrt{1/(n-1)})$, which is effectively the same result as found
 232 by Katz et al. (2006). At this value of θ_m , $S/C^2 = n/(2\sqrt{n-1})$, which is typically $O(1)$.
 233 For example, using $n = 4$, $\theta_m \approx 18^\circ$ and 72° (e.g., see Figure 2) and $S/C^2 = 2/\sqrt{3} \approx 1$.
 234 (Note, however, for $n \leq 2$ the only real angle allowed is $\theta_m = 45^\circ$; see Katz et al. (2006).)
 235 In general the angular and rheological power-law dependence of the least-stable mode does
 236 not change with the introduction of the diffuse interface effect, which itself simply allows
 237 for a finite wavelength $2\pi/k_m$ to be selected. Thus for the least stable angle θ , the least
 238 stable mode is still given by $k_m \approx (Q/D)^{1/4} \gg 1$, and the associated growth rate is
 239 $s_m \approx (1 - \phi_0)b\nu \approx O(1/n)$ (since $b \approx 25/n$).

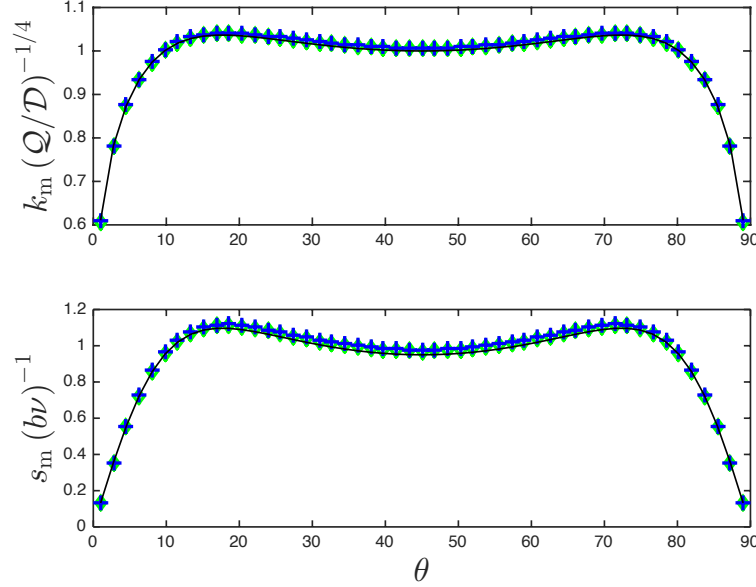


Figure 2: Least stable wavenumber k_m from (21) (top) and associated growth rate s_m from (18) (bottom) versus wave-vector angle θ , for the same cases as in Fig 1 for $\mathcal{D} \neq 0$, shown as green and blue symbols. The thin black curves are the asymptotic relations given in (23); given the proper scaling these relations are sufficient to describe the least stable modes.

4. Discussion and Conclusion: Application to Melt Band experiments

4.1. Scales and numbers for mode selection

The dimensionless numbers for the governing equations depend on various experimental parameters. We consider two cases in the shear-banding experiments of Holtzman et al. (2003, see Table 1) (see also Kohlstedt and Holtzman, 2009): (1) an anorthosite matrix with a low-viscosity MORB (mid-ocean ridge basalt) melt, and (2) an olivine matrix with a high viscosity albite melt, both of which led to shallow shear bands with 15-20° angles, but with significantly different band widths and spacing. For the anorthosite+MORB case, the imposed strain-rate was $\dot{\epsilon}_0 = 3 \times 10^{-4} \text{s}^{-1}$, the matrix viscosity (which we assume to be the same as the basic-state viscosity) was $\mu_0 = 6 \times 10^{11} \text{Pa s}$, the melt viscosity was $\mu_f = 10 \text{Pa s}$, the mean melt volume fraction was $\phi_0 = 0.03$, the matrix permeability was $k = 10^{-17} \text{m}^2$ and the grain-size radius was $r = 2\mu$. In the olivine+albite-melt case,

252 $\dot{\epsilon}_0 = 3 \times 10^{-3} \text{s}^{-1}$, $\mu_0 = 5 \times 10^{12} \text{Pa s}$, $\mu_f = 3.3 \times 10^5 \text{Pa s}$, $\phi_0 = 0.03$, $k = 4 \times 10^{-17} \text{m}^2$,
 253 and $r = 4\mu$.

254 To evaluate our model dimensionless parameters, we use $\mathcal{B}_0 = (1 - \phi_0)^2 B_0 = \frac{4}{3} \mu_0 (1 -$
 255 $\phi_0) / \phi_0$ (see [Bercovici et al., 2001](#); [Bercovici and Ricard, 2003](#)); thus $\mathcal{B}_0 + \frac{4}{3} \mu_0 = \frac{4}{3} \mu_0 / \phi_0$
 256 in which case (17) leads to $\nu = \frac{3}{4} \phi_0$. (Note that our estimates of ν and compaction length
 257 δ differ from that used by [Holtzman et al. \(2003\)](#) who effectively assumed $\mathcal{B}_0 \ll \mu_0$.)

258 For the parameters $\mathcal{Q} = b/\Gamma$ and \mathcal{D} , we use a typical surface tension $\gamma \approx 1 \text{Pa m}$,
 259 $b = 25/n$ ([Mei et al., 2002](#); [Takei and Holtzman, 2009](#)), and $c_0 = \mu_f \phi_0^2 / k$. We can
 260 approximate the microscopic interface area density \mathcal{A}_0 for a mixture of simple spherical or
 261 regular-polyhedral grains of mean size r embedded in a small amount of melt, in which case
 262 $\mathcal{A}_0 \approx 3/r$ ([Bercovici et al., 2001](#); [Bercovici and Ricard, 2012](#); [Ricard and Bercovici, 2009](#)).
 263 As noted already, the microscopic curvature \mathcal{A}_0'' can be positive or negative depending
 264 on whether the mixture self-separates ([Ricard et al., 2001](#)) or undergoes grain-boundary
 265 wetting ([Hier-Majumder et al., 2006](#)), although its sign has no impact on this analysis, since
 266 neither the maximum growth rate s_m nor least stable mode k_m , as given in (23), depend on
 267 \mathcal{A}_0'' . However, the magnitude of \mathcal{A}_0'' is important for estimating the dimensionless numbers
 268 \mathcal{Q} and \mathcal{D} ; in this case we approximate this quantity for that of a spherical grain, in which
 269 case $\mathcal{A}_0'' = 2/r$. Thus using (17),

$$270 \quad \mathcal{Q} = \frac{b}{\Gamma} = \frac{b \mu_0 \dot{\epsilon}_0 r}{\gamma (1 - \phi_0)} \approx 10^4 \text{ and } 10^6 \quad (24a)$$

$$271 \quad \mathcal{D} = \frac{\mu_f \phi_0 r^2}{8 \mu_0 k} \approx 3 \times 10^{-8} \text{ and } 10^{-4} \quad (24b)$$

273 where the two values of each parameter are for the anorthosite+MORB and olivine+albite-
 274 melt experiments, respectively. In estimating \mathcal{Q} , we have assumed diffusion creep, hence
 275 $n = 1$, for lack of any information to the contrary in the experiments. Values of $n > 1$
 276 allow for shallow angled melt bands (i.e., $\theta < 45^\circ$), but only influence mode selection

277 through the relation $b = 25/n$, which would reduce \mathcal{Q} and the growth rate s_m by a factor
278 of n , and the least stable wavenumber k_m by $n^{1/4}$.

279 4.2. Mode selection and comparison to experiments

280 With the dimensionless numbers inferred above, we indeed see that $\mathcal{Q} \gg 1$ and $\mathcal{D} \ll 1$;
281 thus the least stable mode and associated growth rate are given by (23). The dimension-
282 less growth rate for both experimental cases of anorthosite+MORB and olivine+albite-
283 melt is the same (since b and ϕ_0 are the same for each) and yields $s_m \approx 0.5$. For the
284 anorthosite+MORB case, the dimensionless least-stable mode wavenumber is $k_m \approx 800$;
285 thus, given a compaction length $\delta \approx 5000\mu$, the dimensional least-stable mode wavelength
286 is $\lambda_m = 2\pi\delta/k_m \approx 40\mu$. For the olivine+albite-melt case, $k_m \approx 350$ and $\delta \approx 200\mu$, thus
287 $\lambda_m \approx 4\mu$.

288 The melt bands for the anorthosite+MORB experiments were of order 20μ wide, but
289 separated by about 100μ ; for the olivine+albite-melt experiments, the melt bands were a
290 few grains or microns wide, and spaced by about 20μ (Holtzman et al., 2003; Kohlstedt and
291 Holtzman, 2009). The melt-band widths compare favorably with the model predictions for
292 which the band-widths would be $\lambda_m/2$; however, the band spacing is considerably wider
293 than λ_m .

294 The difference between the melt band widths and their spacing in each case indicates
295 two dominant length scales of the instability; this cannot be explained by our linear stability
296 theory, which only predicts one least-stable mode. That the spacing is wider than the band
297 width possibly reflects a nonlinear effect whereby the melt-rich bands drain melt from
298 the surrounding matrix, but only as far away as some larger fraction of the compaction
299 length; however, this assumption needs testing with nonlinear models with our proposed
300 mechanism. Alternatively, the wide spacing could reflect the chemical-diffusion limited
301 instability proposed by Takei and Hier-Majumder (2009) or the effect of finite strain and
302 rotation (e.g., Butler, 2010).

303 The dependence of melt-band width on shear stress indicated in the experiments of
 304 [Holtzman and Kohlstedt \(2007\)](#) also corresponds at least qualitatively to our model pre-
 305 dictions. The relation for the least-stable mode, e.g., (23), implies that band width goes
 306 as $(\text{stress})^{-1/4}$, which is roughly borne out for the “constant rate” (CR) cases – which
 307 are most appropriate for our model – discussed by [Holtzman and Kohlstedt \(2007\)](#), al-
 308 though the data is sparse. [Holtzman and Kohlstedt \(2007\)](#); [Kohlstedt and Holtzman \(2009\)](#)
 309 also documented the relation between melt-band spacing and compaction length, which
 310 is qualitatively in line with our model predictions assuming band spacing and width are
 311 proportional.

312 In the end, the very small experimental melt-band length scales are predicted by our
 313 model to be due to a weak diffuse-interface capillary effect (represented by the dimension-
 314 less number \mathcal{D}), which does not damp growth of the shear-band instability until very large
 315 wave numbers or small wavelengths. Our predictions closely match the narrow experimen-
 316 tal melt-band widths, but more work is needed to understand the wider spacing between
 317 melt bands.

318 **Appendix A. Distribution function and effective curvature near a diffuse interface**

319 In a two-phase mixture, the volume fraction of each phase and the interface between
 320 them is fundamentally described by a distribution, or existence, function Θ which is effec-
 321 tively a spacial box-car function that is unity in one phase and zero in the other. In our
 322 two-phase model, if $\Theta = 1$ for phase 1, then volume fractions and interface density are
 323 (e.g., [Ni and Beckerman, 1991](#); [Bercovici et al., 2001](#))

$$\phi_1 = \frac{1}{\delta V} \int_{\delta V} \Theta dV, \quad \phi_2 = \frac{1}{\delta V} \int_{\delta V} (1 - \Theta) dV \quad \text{and} \quad \mathcal{A} = \frac{1}{\delta V} \int_{\delta V} |\nabla \Theta| dV \quad (\text{A.1})$$

324 where δV is pseudo-infinitesimal volume (i.e., small enough to resolve spatial gradients
 325 but big enough to enclose a statistically meaningful sample of drops, pores and/or grains of

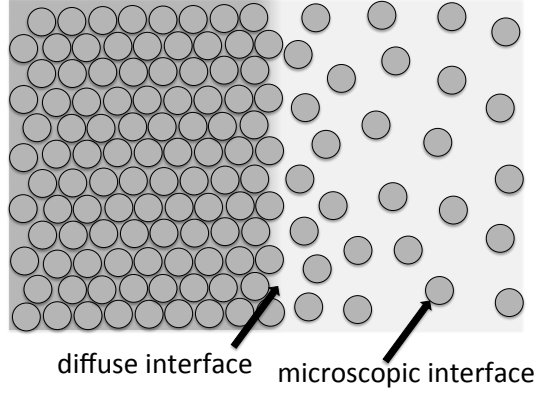


Figure A.1: Simple sketch of an abrupt transition in porosity from packed to dispersed spherical grains (grey circles) in partial melt, to illustrate both microscopic and diffuse interfaces.

the two phases). Typically Θ is assumed to be comprised of fine scale 3-D boxcars whose distribution varies smoothly over δV . Moreover, the effective mean curvature of the fine scale interface is $d\mathcal{A}/d\phi$ (e.g., [Ni and Beckerman, 1991](#); [Bercovici et al., 2001](#)).

However in the melt-band experiments, the final band instabilities are several tens of melt pores and grains wide and that structure is small enough to affect the shape of Θ at an intermediate scale (i.e., between the pore/grain scale and the larger spatial scales resolved by δV). In particular we consider that at this intermediate scale, Θ is influenced by sharp gradients in ϕ , i.e., where the length scale of the gradients becomes comparable to that of the control volume δV and not much bigger than the bubble or grain sizes. Thus, we consider Θ in the vicinity of a mean structure or coherent diffuse-interface imposed by a sharp gradient in ϕ and seek the effective interface curvature near this structure (see [Figure A.1](#)).

Curvature of an interface with unit normal $\hat{\mathbf{n}}$ is simply $\nabla \cdot \hat{\mathbf{n}}$; here we define $\hat{\mathbf{n}}$ to point away from the fluid (where $\Theta = 1$) into the solid matrix (where $\Theta = 0$) and thus $\hat{\mathbf{n}} = -\nabla\Theta/|\nabla\Theta|$ such that the curvature is

$$\kappa = \nabla \cdot \hat{\mathbf{n}} = -\frac{1}{|\nabla\Theta|} \left(\nabla^2\Theta - \frac{\partial^2\Theta}{\partial n^2} \right) \quad \text{where} \quad \frac{\partial^2\Theta}{\partial n^2} = \hat{\mathbf{n}} \cdot \nabla(\hat{\mathbf{n}} \cdot \nabla\Theta) \quad (\text{A.2})$$

341 Following [Sun and Beckermann \(2004\)](#), we next define the mean curvature along the
 342 interface as $\bar{\kappa} = \langle \kappa |\nabla\Theta| \rangle / \langle |\nabla\Theta| \rangle$ where $\langle q \rangle$ is the volume average of any quantity q over
 343 a control volume δV , as described in (A.1). The mean curvature is thus

$$\bar{\kappa} = -\frac{1}{\langle |\nabla\Theta| \rangle} \left\langle \nabla^2\Theta - \frac{\partial^2\Theta}{\partial n^2} \right\rangle = -\frac{1}{\mathcal{A}} \left(\langle \nabla^2\Theta \rangle - \left\langle \frac{\partial^2\Theta}{\partial n^2} \right\rangle \right) \quad (\text{A.3})$$

344 where we have used (A.1) to introduce the factor of $1/\mathcal{A}$. We now consider the two terms
 345 on the far right of (A.3) separately for both a uniform (within a control volume) medium
 346 of dispersed (i.e., non-contacting) identical spherical fluid bubbles, and then also for the
 347 influence of the coherent structure with a sharp porosity gradient. For one bubble of radius
 348 a , $\Theta = 1$ for $r < a$, and $\Theta = 0$ for $r > a$, where r is the radial position from the bubble's
 349 center. In this case

$$\nabla\Theta = -\delta(r-a)\hat{\mathbf{r}}, \quad \nabla^2\Theta = -\frac{2}{r}\delta(r-a) - \delta'(r-a), \quad \text{and} \quad \frac{\partial^2\Theta}{\partial n^2} = \frac{\partial^2\Theta}{\partial r^2} = -\delta'(r-a) \quad (\text{A.4})$$

350 If we have N such bubbles dispersed in the control volume, it can be readily shown that
 351 $\langle |\nabla\Theta| \rangle = \mathcal{A} = N4\pi a^2/\delta V$ as expected, and $\langle \nabla^2\Theta \rangle = 0$ while $\langle \partial^2\Theta/\partial n^2 \rangle = N8\pi a/\delta V$.
 352 In total, the microscopic contribution to the mean curvature $\bar{\kappa}$ is simply $2/a$, but only the
 353 second term on the far right of (A.3) contributes to the mean microscopic curvature.

354 In the vicinity of a coherent structure with a sharp gradient in ϕ , $\langle \nabla^2\Theta \rangle = \nabla^2\phi$ (pro-
 355 vided that $\nabla\Theta$ averaged over any surface element of the control volume δV varies no
 356 more than linearly perpendicular to that element; see [Bercovici et al., 2001](#)). Moreover, the
 357 control volume can be chosen small enough to render the coherent structure a flat diffuse
 358 surface or boundary layer inside that volume; since $\partial^2\Theta/\partial n^2$ is an odd function centered
 359 on that structure, then $\langle \partial^2\Theta/\partial n^2 \rangle = 0$.

360 Summing the effects of the microscopic and coherent structures together, we see that
 361 only the coherent structure contributes to the first term on the far right side of (A.3), while

only the microscopic structure contributes to the second term. Therefore, the final average curvature (A.3) associated with both the microscopic background value and that due to the coherent structure is

$$\frac{d\alpha}{d\phi} = \bar{\kappa} = \frac{d\mathcal{A}}{d\phi} - \frac{1}{\mathcal{A}} \nabla^2 \phi \quad (\text{A.5})$$

where we have associated $d\mathcal{A}/d\phi$ with the mean microscopic curvature $2/a$, and we note that (A.5) is the same as that derived by Sun and Beckermann (2004). In the end, we infer that with both finer and coarse scale structures in the distribution function Θ , the effective interface curvature is given by (A.5), which is the starting point for our model with equation (1).

Acknowledgments. The authors sincerely thank Sam Butler and Ben Holtzman for thoughtful reviews. Support was provided by the National Science Foundation (NSF, grant EAR-1344538), the Natural Environment Research Council (NERC, grant NE/I023929/1) and Trinity College.

References

- Aharonov, E., Spiegelman, M., Kelemen, P., 1997. Three-dimensional flow and reaction in porous media: Implications for the earth’s mantle and sedimentary basins. *J. Geophys. Res.* 102, 14821–14834.
- Alisic, L., Rudge, J. F., Katz, R. F., Wells, G. N., Rhebergen, S., 2014. Compaction around a rigid, circular inclusion in partially molten rock. *Journal of Geophysical Research: Solid Earth* 119 (7), 5903–5920.
<http://dx.doi.org/10.1002/2013JB010906>
- Anderson, D. M., McFadden, G. B., Wheeler, A. A., 1998. Diffuse-interface methods in fluid mechanics. *Annual Review of Fluid Mechanics* 30 (1), 139–165.
<http://dx.doi.org/10.1146/annurev.fluid.30.1.139>

- 385 Bercovici, D., Ricard, Y., 2003. Energetics of a two-phase model of lithospheric damage,
386 shear localization and plate-boundary formation. *Geophys. J. Intl.* 152, 581–596.
- 387 Bercovici, D., Ricard, Y., 2012. Mechanisms for the generation of plate tectonics by two-
388 phase grain-damage and pinning. *Phys. Earth Planet. Int.* 202-203, 27–55.
- 389 Bercovici, D., Ricard, Y., Schubert, G., 2001. A two-phase model of compaction and dam-
390 age, 1. general theory. *J. Geophys. Res.* 106 (B5), 8887–8906.
- 391 Butler, S., 2010. Porosity localizing instability in a compacting porous layer in a pure shear
392 flow and the evolution of porosity band wavelength. *Physics of the Earth and Planetary*
393 *Interiors* 182 (1–2), 30 – 41.
394 [http://www.sciencedirect.com/science/article/pii/](http://www.sciencedirect.com/science/article/pii/S003192011000124X)
395 [S003192011000124X](http://www.sciencedirect.com/science/article/pii/S003192011000124X)
- 396 Butler, S. L., 2012. Numerical models of shear-induced melt band formation with
397 anisotropic matrix viscosity. *Phys. Earth Planet Int.* 200-201, 28–36.
- 398 Chen, L.-Q., 2002. Phase-field models for microstructure evolution. *Annual Review of*
399 *Materials Research* 32 (1), 113–140.
400 <http://dx.doi.org/10.1146/annurev.matsci.32.112001.132041>
- 401 Cox, K., McKenzie, D., White, R., 1993. Melting and melt movement in the Earth. Oxford
402 University Press, New York, NY, first published in *Phil. Trans. R. Soc.*, Ser. A, vol.342,
403 pp1–91.
- 404 Daines, M. J., Kohlstedt, D. L., 1997. Influence of deformation on melt topology in peri-
405 dotites. *J. Geophys. Res* 102, 10257–10271.
- 406 Gerya, T. V., 2013. Three-dimensional thermomechanical modeling of oceanic spreading
407 initiation and evolution. *Physics of the Earth and Planetary Interiors* 214 (0), 35 – 52.

408 [http://www.sciencedirect.com/science/article/pii/](http://www.sciencedirect.com/science/article/pii/S0031920112001835)
 409 [S0031920112001835](http://www.sciencedirect.com/science/article/pii/S0031920112001835)

410 Gerya, T. V., Meilick, F. I., 2011. Geodynamic regimes of subduction under an active
 411 margin: effects of rheological weakening by fluids and melts. *Journal of Metamorphic*
 412 *Geology* 29 (1), 7–31.
 413 <http://dx.doi.org/10.1111/j.1525-1314.2010.00904.x>

414 Hier-Majumder, S., Ricard, Y., Bercovici, D., 2006. Role of grain boundaries in magma
 415 migration and storage. *Earth Planet Sci. Lett.* 248, 735–749.

416 Holtzman, B. K., Groebner, N. J., Zimmerman, M. E., Ginsberg, S. B., Kohlstedt, D. L.,
 417 2003. Stress-driven melt segregation in partially molten rocks. *Geochemistry, Geo-*
 418 *physics, Geosystems* 4 (5), doi:10.1029/2001GC000258.
 419 <http://dx.doi.org/10.1029/2001GC000258>

420 Holtzman, B. K., Kohlstedt, D. L., 2007. Stress-driven melt segregation and strain
 421 partitioning in partially molten rocks: Effects of stress and strain. *Journal of Petrology*
 422 48 (12), 2379–2406.
 423 [http://petrology.oxfordjournals.org/content/48/12/2379.](http://petrology.oxfordjournals.org/content/48/12/2379.abstract)
 424 [abstract](http://petrology.oxfordjournals.org/content/48/12/2379.abstract)

425 Katz, R. F., 2008. Magma Dynamics with the Enthalpy Method: Benchmark Solutions and
 426 Magmatic Focusing at Mid-ocean Ridges. *J. Petrol.* 49 (12), 2099–2121.

427 Katz, R. F., Spiegelman, M., Holtzman, B., 08 2006. The dynamics of melt and shear
 428 localization in partially molten aggregates. *Nature* 442 (7103), 676–679.
 429 <http://dx.doi.org/10.1038/nature05039>

430 Katz, R. F., Takei, Y., 2013. Consequences of viscous anisotropy in a deforming, two-phase
 431 aggregate. part 2. numerical solutions of the full equations. *J. Fluid Mech.* 734, 456–485.

- 432 King, D. S., Hier-Majumder, S., Kohlstedt, D. L., 2011. An experimental study of the
433 effects of surface tension in homogenizing perturbations in melt fraction. *Earth and*
434 *Planetary Science Letters* 307 (3–4), 349 – 360.
435 [http://www.sciencedirect.com/science/article/pii/](http://www.sciencedirect.com/science/article/pii/S0012821X11002809)
436 [S0012821X11002809](http://www.sciencedirect.com/science/article/pii/S0012821X11002809)
- 437 King, D. S. H., Zimmerman, M. E., Kohlstedt, D. L., 2010. Stress-driven melt segregation
438 in partially molten olivine-rich rocks deformed in torsion. *J. Petrol.* 51, 21–42.
- 439 Kohlstedt, D. L., Holtzman, B. K., 2009. Shearing melt out of the earth: An experimental-
440 ist's perspective on the influence of deformation on melt extraction. *Ann* 37, 561–593.
- 441 McKenzie, D., 1984. The generation and compaction of partially molten rock. *J. Petrol.* 25,
442 713–765.
- 443 Mei, S., Bai, W., Hiraga, T., Kohlstedt, D., 2002. Influence of melt on the creep behavior of
444 olivine–basalt aggregates under hydrous conditions. *Earth and Planetary Science Letters*
445 201 (3–4), 491 – 507.
446 [http://dx.doi.org/10.1016/S0012-821X\(02\)00745-8](http://dx.doi.org/10.1016/S0012-821X(02)00745-8)
- 447 Moelans, N., Blanpain, B., Wollants, P., 2008. An introduction to phase-field modeling
448 of microstructure evolution. *Calphad* 32 (2), 268–294.
449 <http://dx.doi.org/10.1016/j.calphad.2007.11.003>
- 450 Ni, J., Beckerman, C., 1991. A volume-averaged two-phase model for transport phenomena
451 during solidification. *Metall. Trans. B* 22, 349–361.
- 452 Parsons, R., Nimmo, F., Hustoft, J., Holtzman, B., Kohlstedt, D., 2008. An experimental
453 and numerical study of surface tension-driven melt flow. *Earth and Planetary Science*
454 *Letters* 267 (3–4), 548 – 557.

455 [http://www.sciencedirect.com/science/article/pii/](http://www.sciencedirect.com/science/article/pii/S0012821X07008023)
456 [S0012821X07008023](http://www.sciencedirect.com/science/article/pii/S0012821X07008023)

457 Qi, C., Zhao, Y.-H., Kohlstedt, D. L., 2013. An experimental study of pressure shadows in
458 partially molten rocks. *Earth. Planet. Sci. Lett.* 382, 77–84.

459 Ricard, Y., Bercovici, D., 2009. A continuum theory of grain size evolution and damage. *J.*
460 *Geophys. Res.* 114, B01204, doi:10.1029/2007JB005491.

461 Ricard, Y., Bercovici, D., Schubert, G., 2001. A two-phase model of compaction and dam-
462 age, 2, applications to compaction, deformation, and the role of interfacial surface ten-
463 sion. *J. Geophys. Res.* 106 (B5), 8907–8924.

464 Rudge, J. F., Bercovici, D., 2015. Melt-band instabilities with two-phase grain-damage.
465 *Geophys. J. Int.* 201, 640–651.

466 Spiegelman, M., 2003. Linear analysis of melt band formation by simple shear. *Geochem.*
467 *Geophys. Geosyst.* 4, 8615.

468 Spiegelman, M., McKenzie, D., 1987. Simple 2-d models for melt extraction at mid-ocean
469 ridges and island arcs. *Earth Planet. Sci. Lett.* 83, 137–152.

470 Stevenson, D., 1986. On the role of surface tension in the migration of melts and fluids.
471 *Geophys. Res. Lett.* 13, 1149–1152.

472 Stevenson, D. J., 1989. Spontaneous small-scale melt segregation in partial melts undergo-
473 ing deformation. *Geophys. Res. Lett.* 16, 1067–1070.

474 Sun, Y., Beckermann, C., 2004. Diffuse interface modeling of two-phase flows based on
475 averaging: mass and momentum equations. *Physica D* 198, 281–308.

476 Takei, Y., Hier-Majumder, S., 10 2009. A generalized formulation of interfacial tension
477 driven fluid migration with dissolution/precipitation. *Earth and Planetary Science Letters*

478 288 (1–2), 138–148.

479 <http://dx.doi.org/10.1016/j.epsl.2009.09.016>

480 Takei, Y., Holtzman, B., 2009. Viscous constitutive relations of solid-liquid composites in
481 terms of grain boundary contiguity: 3. Causes and consequences of viscous anisotropy.
482 J. Geophys. Res. 114, B06207.

483 Takei, Y., Katz, R. F., 2013. Consequences of viscous anisotropy in a deforming, two-
484 phase aggregate. part 1. governing equations and linearized analysis. J. Fluid Mech. 734,
485 424–455.